

Localization and Surface Characterization by Zhurong Mars Rover at Utopia Planitia

Liang Ding (✉ liangding@hit.edu.cn)

State Key Laboratory of Robotics and System, Harbin Institute of Technology <https://orcid.org/0000-0002-8351-5178>

Ruyi Zhou

State Key Laboratory of Robotics and System, Harbin Institute of Technology <https://orcid.org/0000-0002-1854-9451>

Tianyi Yu

Beijing Aerospace Control Center

Haibo Gao

Harbin Institute of Technology

Huaiguang Yang

State Key Laboratory of Robotics and System, Harbin Institute of Technology

Jian Li

Beijing Aerospace Control Center

Ye Yuan

State Key Laboratory of Robotics and System, Harbin Institute of Technology

Chuankai Liu

Beijing Aerospace Control Center

Jia Wang

Beijing Aerospace Control Center

Yuyan Zhao

Institute of Geochemistry Chinese Academy of Sciences <https://orcid.org/0000-0003-2551-5425>

Zhengyin Wang

State Key Laboratory of Robotics and System, Harbin Institute of Technology

Xiyu Wang

Center for Lunar and Planetary Sciences, Institute of Geochemistry, Chinese Academy of Science;
University of Chinese Academy of Sciences

Gang Bao

Center for Lunar and Planetary Sciences, Institute of Geochemistry, Chinese Academy of Science;
University of Chinese Academy of Sciences

Zongquan Deng

State Key Laboratory of Robotics and System, Harbin Institute of Technology

Lan Huang

State Key Laboratory of Robotics and System, Harbin Institute of Technology

Nan Li

State Key Laboratory of Robotics and System, Harbin Institute of Technology

Xiaofeng Cui

Beijing Aerospace Control Center

Ximing He

Beijing Aerospace Control Center

Yang Jia

Beijing Institute of Spacecraft System Engineering

Baofeng Yuan

Beijing Institute of Spacecraft System Engineering

Guangjun Liu

Department of Aerospace Engineering, Ryerson University

Hui Zhang

Beijing Aerospace Control Center

Rui Zhao

Beijing Aerospace Control Center

Zuoyu Zhang

Beijing Aerospace Control Center

Ziqing Cheng

Beijing Aerospace Control Center

Fan Wu

Beijing Aerospace Control Center

Qian Xu

Beijing Aerospace Control Center

Hao Lu

Beijing Aerospace Control Center

Lutz Richter

Large Space Structures (LSS)

Zhen Liu

State Key Laboratory of Robotics and System, Harbin Institute of Technology

Fuliang Niu

State Key Laboratory of Robotics and System, Harbin Institute of Technology

Huanan Qi

State Key Laboratory of Robotics and System, Harbin Institute of Technology

Shu Li

State Key Laboratory of Robotics and System, Harbin Institute of Technology

Wenhai Feng

State Key Laboratory of Robotics and System, Harbin Institute of Technology

Chaojie Yang

State Key Laboratory of Robotics and System, Harbin Institute of Technology

Baichao Chen

Beijing Institute of Spacecraft System Engineering

Zhaolong Dang

Beijing Institute of Spacecraft System Engineering

Mingming Zhang

Center for Lunar and Planetary Sciences, Institute of Geochemistry, Chinese Academy of Science;
University of Chinese Academy of Sciences

Lichun Li

Beijing Aerospace Control Center

Xiaoxue Wang

Beijing Aerospace Control Center

Zhao Huang

Beijing Aerospace Control Center

Jitao Zhang

Beijing Aerospace Control Center

Hongjun Xing

State Key Laboratory of Robotics and System, Harbin Institute of Technology

Guanyu Wang

State Key Laboratory of Robotics and System, Harbin Institute of Technology

Lizhou Niu

State Key Laboratory of Robotics and System, Harbin Institute of Technology

Peng Xu

State Key Laboratory of Robotics and System, Harbin Institute of Technology

Wenhui Wan

State Key Laboratory of Remote Sensing Science, Aerospace Information Research Institute, Chinese
Academy of Sciences

Kaichang Di

State Key Laboratory of Remote Sensing Science, Institute of Remote Sensing and Digital Earth, Chinese
Academy of Sciences, Beijing 100101, China

Article

Keywords: Mars rover, Mars, Utopia Planitia, Zhurong rover

Posted Date: September 24th, 2021

DOI: <https://doi.org/10.21203/rs.3.rs-836162/v1>

License:  This work is licensed under a Creative Commons Attribution 4.0 International License.

[Read Full License](#)

Version of Record: A version of this preprint was published at Nature Geoscience on March 7th, 2022. See the published version at <https://doi.org/10.1038/s41561-022-00905-6>.

Localization and Surface Characterization by Zhurong Mars Rover at Utopia Planitia

L. Ding^{1*}†, R. Zhou^{1†}, T. Yu^{2†}, H. Gao^{1*}, H. Yang^{1*}, J. Li², Y. Yuan¹, C. Liu², J. Wang², Y. Zhao^{3,4}, Z. Wang¹, X. Wang^{3,5}, G. Bao^{3,5}, Z. Deng¹, L. Huang¹, N. Li¹, X. Cui², X. He², Y. Jia⁶, B. Yuan⁶, G. Liu⁷, H. Zhang², R. Zhao², Z. Zhang², Z. Cheng², F. Wu², Q. Xu², H. Lu², L. Richter⁸, Z. Liu¹, F. Niu¹, H. Qi¹, S. Li¹, W. Feng¹, C. Yang¹, B. Chen⁶, Z. Dang⁶, M. Zhang^{3,5}, L. Li², X. Wang², Z. Huang², J. Zhang², H. Xing¹, G. Wang¹, L. Niu¹, P. Xu¹, W. Wan⁹, K. Di⁹

¹*State Key Laboratory of Robotics and System, Harbin Institute of Technology; Harbin 150080, China.*

²*Beijing Aerospace Control Center; Beijing 100094, China.*

³*Center for Lunar and Planetary Sciences, Institute of Geochemistry, Chinese Academy of Science,*

10 *Guiyang 550081, China.*

⁴*CAS Center for Excellence in Comparative Planetology, Hefei 230026, China.*

⁵*University of Chinese Academy of Sciences, Beijing 100049, China.*

⁶*Beijing Institute of Spacecraft System Engineering; Beijing 100094, China.*

⁷*Department of Aerospace Engineering, Ryerson University; Toronto, ON M5B 2K3, Canada.*

15 ⁸*Large Space Structures (LSS), Hauptstrasse 1e, Eching, Germany.*

⁹*State Key Laboratory of Remote Sensing Science, Aerospace Information Research Institute, Chinese Academy of Sciences; Beijing 100101, China.*

*Corresponding author. Email: liangding@hit.edu.cn (L. D.), gaohaibo@hit.edu.cn (H. G.), yanghuaiguang_hit@163.com (H. Y.).

20 †These authors contributed equally to this work

China's first Mars rover, Zhurong, has successfully touched down on the southern Utopia Planitia of Mars at 109.925° E, 25.066° N, and since performed cooperative multiscale investigations with the Tianwen-1 orbiter. Here we present primary localization and surface characterization results based on complementary data of the first 60 sols. The Zhurong rover has traversed 450.9 m southwards over a flat surface with mild wheel slippage (less than 0.2 in slip ratio). The encountered crescent-shaped sand dune indicates a NE-SW local wind direction, consistent with larger-range remote-sensing observations. Soil parameter analysis based on terramechanics indicates that the topsoil has high bearing strength and cohesion, and its equivalent stiffness and internal friction angle are ~1390–5872 kPa·m⁻ⁿ and ~21°–34° respectively. Rocks observed strewn with dense pits, or showing layered and flaky structures, are presumed to be involved in physical weathering like severe wind erosion and potential chemical weathering processes. These preliminary observations suggest great potential of in-situ investigations by the scientific payload suite of the Zhurong rover in obtaining new clues of the region's aeolian and aqueous history. Cooperative investigations using the related payloads on both the rover and the obiter could peek into the habitability evolution of the northern lowlands on Mars.

The Mars Exploration Probe Tianwen-1 lander (including the Zhurong rover) has landed on the Utopia Planitia of Mars on May 15, 2021¹ and successfully fulfilled the goals of ‘orbiting, landing, and roving’ on Mars at China’s first independent attempt. The Zhurong rover (1230×830×540 mm, 240 kg; Extended Data Fig. 1), a six-wheeled solar-powered robot with active suspension, working in high locomotive performance (Extended Data Table 1) and carrying six scientific payloads^{2–7}, becomes one of the most powerful rovers to date that ever landed on the Northern Plain of Mars. Zhurong has been roving and conducting *in-situ* investigations for more than the designed 90-sols primary mission, collaborating with the orbiter to collect complementary scientific data at different perception scales and precisions for five primary scientific objectives⁷. Scientific data of ~7 Gbit has been relayed back via the Tianwen-1 orbiter

and is currently under calibration. Here we present preliminary results in terms of the localization and surface characterization of the landing site based on the first 60-sols cooperative observations from the Zhurong rover and the Tianwen-1 orbiter.

The landing site location was refined to 109.925° E, 25.066° N using the descent image sequence and mapped to the orbiter-derived digital elevation map (DEM) at an elevation of -4099.8 m. It was further confirmed by the High-Resolution Imaging Science Experiment (HiRISE) onboard the Mars Reconnaissance Orbiter (MRO; Extended Data Fig. 2), in which the lander and rover can be identified. The landing site (Fig. 1a) lies in the Late Hesperian lowland unit, dated to $\sim 3.32\text{--}3.36$ Ga⁸. The region contains hundreds of superposed pedestal-crater forms, a thumbprint terrain, topographically-subdued wrinkle ridges, and narrow grabens northeast of Alba Mons⁹. We highlight the local area in a circular shape that might be within reach of the rover (centred on 109.925° E, 24.980° N; diameter = 20 km; Fig. 1b). The elevation of the local area gradually increasing due south from -4219 to -3989 m, with an average elevation of -4095 m and a standard deviation of 42.11 m (based on the Mars Orbiter Laser Altimeter (MOLA) DEM 128PPD; 463 m·pixel⁻¹). About 99% of the area consist of slope less than 2.3° , and relatively large slopes are primarily distributed at the rim of impact craters (Fig. 1c). Therefore, the area is flat and may facilitate the long-distance roving and exploration of the Zhurong rover.

Zhurong has traveled 450.9 m due south during the first 60 sols (Fig. 2a), with waypoints calculated by cross-site visual localization¹⁰, and conducted several *in-situ* investigations (Extended Data Table 2). An off-line dynamic locomotion simulation¹¹ (Extended Data Fig. 3) implemented on the Rover Simulation based on Terramechanics Dynamics (RoSTDyn)¹² is used to evaluate and verify the safety and efficiency of the planned path. Compared with the visual localization postures, the simulations of planned traverses deviated by $\leq 2\%$, and the average azimuth error was $\leq 1^\circ$. Due to the inevitable wheel slippage, the planned destination was not always accurately reached, particularly when traversing through drifting soils. The wheel slip ratio (denoted by s) over each continuous steady traverse is calculated using the Guidance,

Navigation and Control System (GNC)-derived rover velocity and the wheel angular velocity derived from the encoder (see Methods). The distribution of the wheel slip ratio along the route (Fig. 2b) shows that the Zhurong rover primarily operates under mild wheel slippage ($s < 0.2$). The average slip ratio of a steady climb of $\sim 0.55^\circ$ was 0.056, consistent with the elevation increase of 4.34 m during the 60-sol journey (Fig. 5 2c). The largest average slip ratio of 0.22 occurred on sol 55 while Zhurong climbed a slope of $\sim 1.14^\circ$. Occasionally, the rover suffers wheel skids ($s < 0$) on localized down slopes, e.g., traversing through a small down-slope area of $\sim -3^\circ$ on sol 34 before approaching a crescent-shaped dune. Wheel tracks in periodic textures (Extended Data Fig. 4a) left by the Zhurong rover also provide clues on the severity of wheel slippage in a more detailed view. By extracting the wheel track unit (see Methods), the average 10 wheel slip ratio on legible parts of the wheel track (being created after Zhurong traversed from waypoints X to A; Extended Data Fig. 4b) was calculated to be 0.05, consistent with telemetry-derived results.

The first 360° panorama is stitched from twelve images taken by the Navigation and Terrain Camera (NaTeCam) (Fig. 3a). The panorama shows an overview of gentle topography at the landing site, with major surface geological features including aeolian dunes, small craters, and rocks. One distinct feature is 15 that the distribution of several aeolian dunes with ripple-like structures, which can be reached and investigated by the rover. Most dunes in this area are bright-toned and crescent-shaped, with windward slopes (the protruding side) oriented approximately north-eastwards, indicating a NE-SW local wind direction (Extended Data Fig. 2b). The first dune encountered by the Zhrong rover on sol 50 is 40 m in length, 8 m in width, and 0.6 m in height (Fig. 3b), with sands in two different colors covered the dune 20 surface. Several seagull-shaped deposits are usually formed from two merged dunes, and one approximate to a line as shown in the enlarged view (Extended Data Fig. 2b). Further scientific observations from the orbit are needed to determine whether these dunes are currently active. A fresh mini crater (~ 0.95 m in diameter) beneath the lander created by the landing plume was observed in the NaTeCam image, providing clues on a shallow subsurface layer (Fig. 3c). Gravels (1–4 cm in diameter), splashed out around the lander

struts or settled on the crater rim, exhibit a dark-brown tone and in sharp contrast to the semi-buried ones by the dust.

The mechanical properties of the surface soils (Fig. 3d) are estimated using the lugged wheels of Zhurong as test devices. Using stereo images taken by the rear Hazard-avoidance Camera (HazCam), the 5 soil surface deformation by lugged wheels can be reconstructed and the wheel sinkage can be estimated by extracting the wheel track profile, as it was done for the Chang'E-3 mission¹³. In legible parts of the wheel tracks (Extended Data Fig. 4d), the equivalent wheel sinkage (the sum of the contribution of the lug and the drum-shaped wheel) was approximated to be 10 mm. However, most wheel tracks are incomplete without well-trimmed contours (Extended Data Fig. 4e). The wheel tracks are formed in a way that the 5-mm-high 10 wheel lugs almost completely immerse into the soil, with the wheel rim several millimetres above the surface (as observed in the images on sol 12 taken by a wireless camera deployed on the ground; Extended Data Fig. 4c). Therefore, the equivalent wheel sinkage was estimated to be about 5 mm. Wheel sinkage is sometimes interrupted by protruding gravels on the surface , leading to smaller values (about 2 mm) or going larger to approximately 15 mm when the wheel rim sinks below the surface (Extended Data Fig. 4f).

15 Compared with Yutu or Yutu-2 rovers of the lunar exploration missions, the load on each wheel of Zhurong (~148.8 N) is much larger than that on the wheels of lunar rovers (~36.5 N). However, the corresponding wheel sinkage during the Zhurong traverses was not more significant, indicating a greater bearing strength of the Martian soil than that of the lunar regolith. According to the terramechanics model¹⁴ for the lugged wheels, characteristic curves of the sinkage exponent (denoted by n) and the equivalent 20 stiffness (denoted by K_s) were predicted under different sinkage conditions (Fig. 4a). We set the upper bound of n to 1.0 (i.e., the typical value of lunar regolith¹⁵). As n increases, the corresponding soil softens and results in a sharp increase in wheel sinkage. Also, the lower bound of n is set to 0.7 to maintain K_s within the reasonable range because the K_s decreases with a decresing n value. Considering soil characteristics within curves corresponding to a wheel sinkage of 2-5 mm and representative terrestrial soil

types, the equivalent stiffness K_s was estimated to be 1390–5872 kPa·mⁿ, shown as the rectangular region in Fig. 4a.

Using the wheel-terrain interaction model, the characteristic shearing curves under different driving torques (4.0–8.0 N·m) were predicted (Fig. 4b). Transformed from the wheel driving motor current in moving states, the average wheel driving torque during each continuous traverse during sols 23–34 ranged 3.7–7.0 N·m (Extended Data Table 3). The maximum wheel driving torque reached 8–10 N·m during some sampling periods, although the corresponding slip ratio increased accordingly. Therefore, 8 N·m was taken as the upper bound of the driving torque. Taking the cohesion (denoted by c) of 6 kPa (the upper bound; close to the maximum soil cohesion from North Gower clayey¹⁶ loam in a reasonable range), and 1.5 kPa (the lower bound; the minimum cohesion of representative soil types on Earth) respectively, the internal friction angle (denoted by φ) was limited to ~21°–34° in the area enclosed by these curves. The friction characteristics of the soil at the Tianwen-1 site are inferior to those of the InSight, Phoenix, and Mars Pathfinder landing sites. Meanwhile, the soil cohesion of the Tianwen-1 site is relatively large, resulting in soil adhering to the wheel surface during the traverse (Extended Data Fig. 4c). Compared with the soil shearing properties in other Mars missions^{17–23}, the in-situ results of Tianwen-1 are within the envelop region of others and closest to that of the Viking 1, and Curiosity sites (Fig. 4c).

The flat nature of the landing area is occasionally interrupted by small craters. More than 2000 craters were identified on the HiRISE image (spatial resolution ~0.3 m) within the circular area surrounding the Tianwen-1 site (centred on 109.925° E, 25.048° N; diameter = 3 km; Extended Data Fig. 5a), and a size-frequency distribution analysis (Extended Data Fig. 5b) was conducted. The crater diameter in the area ranges from 1.1 and 287.6 m, with a mean diameter of 10.6 m. About 79% of these craters are ≤ 10 m in diameter, and most are likely secondary craters. Relatively large craters (≥ 200 m in diameter) (as C1, C2, C3 in Extended Data Fig. 5a) show clear impact structures but had broken or degraded rims. Craters that

Zhurong has encountered are relatively small (< 10 m in diameter) (Extended Data Fig. 5c, d) in a depression-shape, surrounded by dark rocks (probably ejecta). Aeolian deposits within the craters may indicate that the craters may be subject to long-term weathering.

The surface is primarily free of large boulders but is scattered with small rocks and clasts bearing 5 distinct features (Extended Data Fig. 6). Most rocks are fine-grained in texture and angular to subangular, with low roundness in morphology. Some rocks with pitted surfaces show similar morphology to igneous rocks as observed in previous missions (e.g., by the Viking-1 lander and the Spirit rover)^{24,25}, which are proposed to form via brine-related dissolution processes under cold environments^{25,26}. Similar rock features 10 may provide insights into the climate and geological processes of the Tianwen-1 site but require detailed investigations by the scientific payloads of the rover. Some rock chucks also show flaky texture, similar to the rock targets observed at Gusev Plain, such as “Mimi”²⁷. The flake textures might be related to aqueous alterations that dew water goes through insolation cracking to flake the rocks, and brine and salt may work 15 to cement these flakes²⁸. In addition, rocks with grooves and etchings on the windward sides are ubiquitous on the landing site, usually interpreted as ventifacts resulting from intense wind erosion with aeolian particles²⁹⁻³¹. Therefore, the rock textures observed at the site so far may indicate both presences of physical weathering (e.g., impact sputtering, wind erosion, and potential freeze-thaw weathering) and aqueous interactions, involving salt and brine activities. These rock and soil targets provide excellent 20 opportunities to peek into the aqueous history and climate evolution of the northern lowlands and shed light on the habitability evolution of Mars.

20 References

1. Mallapaty S. *Nature* **593**, 323–324 (2021).
2. Li, C. *et al.* Scientific objectives and payload configuration of China’s first mars exploration mission. *J. Deep Space Explor.* **5**, 5 (2018).

3. Liang, X. *et al.* The navigation and terrain cameras on the Tianwen-1 Mars rover, *Space Sci. Rev.* **217**, 37 (2021).
4. Zhou, B. *et al.* The Mars rover subsurface penetrating radar onboard China's Mars 2020 mission, *Earth Planet. Phys.* **4**, 345–354 (2020).
5. Peng, Y. *et al.* Overview of the Mars climate station for Tianwen-1 mission, *Earth Planet. Phys.* **4**, 371–383 (2020).
6. Du, A. *et al.* The Chinese Mars rover fluxgate magnetometers, *Space Sci. Rev.* **216**, 135 (2020).
7. Li, C. *et al.* Design and realization of Chinese Tianwen-1 energetic particle analyzer, *Space Sci. Rev.* **217**, 26 (2020).
10. Wu, B. *et al.* Characterization of the candidate landing region for Tianwen-1–China's first mission to Mars, *Earth Space Sci.* **8**, e2021EA001670 (2021).
9. Tanaka, K.L. *et al.* Geologic map of Mars: U.S. Geological Survey Scientific Investigations Map 3292, (US Geological Survey, 2014).
10. Liu, S. *et al.* High precision landing site mapping and rover localization for Chang'e-3 mission. *Sci. China Phys. Mech. Astron.* **58**, 1–11 (2015).
15. Yang, H. *et al.* paper presented in the 2018 IEEE International Conference on Robotics and Automation, Brisbane, QLD, Australia, 21 to 25 May 2018.
12. Li, W., Ding, L., Gao, H., Deng, Z., Li, N. ROSTDyn: Rover simulation based on terramechanics and dynamics. *J. Terramech.* **50**, 199–210 (2013).
20. 13. Gao, Y., Spiteri, C., Li, C., Zheng, Y. Lunar soil strength estimation based on Chang'E-3 images. *Adv. Space Res.* **58**, 1893–1899 (2016).
14. Ding, L. *et al.* Interaction mechanics model for rigid driving wheels of planetary rovers moving on sandy terrain with consideration of multiple physical effects. *J. Field Robot.* **32**, 827–859 (2015).

15. French, B. M., Heiken, G., Vaniman D. *Lunar Sourcebook: A User's Guide to the Moon* (Cambridge University Press, Cambridge, 1991)
16. Wong, J.Y. *Theory of Ground Vehicles* (John Wiley & Sons, New Jersey, 2008).
17. Henry, J., Bruce, M. Viking landing sites, remote-sensing observations, and physical properties of
5 Martian surface materials. *Icarus* **81**, 164–184 (1989).
18. Rover team, Characterization of the martian surface deposits by the Mars Pathfinder rover, Sojourner. *Science* **278**, 1765–1768 (1997).
19. Arvidson, R. E. *et al.* Localization and physical properties experiments conducted by Spirit at Gusev Crater. *Science* **305**, 821–824 (2004).
- 10 20. Arvidson, R. E. *et al.* Localization and physical property experiments conducted by Opportunity at Meridiani Planum. *Science* **306**, 1730–1733 (2004).
21. Arvidson, R. E. *et al.* Terrain physical properties derived from orbital data and the first 360 sols of Mars Science Laboratory Curiosity rover observations in Gale Crater. *J. Geophys. Res. Planets.* **119**, 1322–1344 (2013).
- 15 22. Any, S. *et al.* Phoenix soil physical properties investigation. *J. Geophys. Res.* **114**, E00E0 (2009).
23. Golombek, M. *et al.* Geology of the InSight landing site on Mars. *Nat. Commun.* **11**, 1014 (2020).
24. Mutch, T. A. *et al.* The surface of Mars: The View from the Viking 1 lander. *Science* **193**, 4255, 791–801 (1976)
25. Head, J. M., Kreslavsky, A., Marchant, D. R. Pitted rock surfaces on Mars: a mechanism of formation
20 by transient melting of snow and ice. *J. Geophys. Res.* **116**, E09007 (2011).
26. Cabrol, N. A. *et al.* Aqueous processes at Gusev crater inferred from physical properties of rocks and soils along the Spirit traverse. *J. Geophys. Res. Planets.* **111**, E02S20 (2006).

27. Arvidson, R. E., *et al.* Overview of the Spirit Mars Exploration Rover Mission to Gusev Crater: Landing site to Backstay Rock in the Columbia Hills, *J. Geophys. Res.*, **111**, E02S01 (2006).
28. Thomas, M., Clarke, J., Pain, C. Weathering, erosion and landscape processes on Mars identified from recent rover imagery, and possible Earth analogues. *Aust. J. Earth Sci.* **52**, 365–378 (2005).
- 5 29. Greeley, R. *et al.* Gusev Crater: Wind-related features and processes observed by the Mars Exploration Rover Spirit. *J. Geophys. Res.-Atmos.* **111**, E02S09 (2006).
30. Thomson, B. J., Bridges, N. T., Greeley, R. Rock abrasion features in the Columbia Hills, Mars. *J. Geophys. Res. Planets.* **113**, E08010 (2008).
31. Bridges, N. T. *et al.* Ventifacts at the Pathfinder landing site. *J. Geophys. Res. Planets.* **104**, 8595–8615
10 (1999).

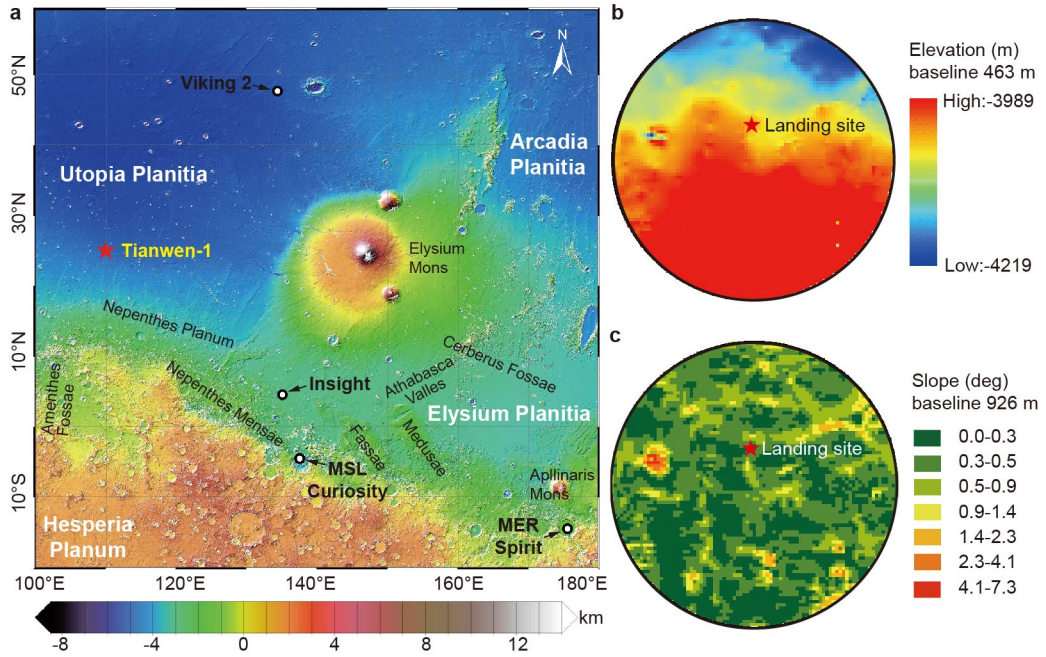


Fig. 1. Regional topographic map of the Tianwen-1 landing site. **a**, The Tianwen-1 landing site is at the southern Utopia Planitia, Mars. The map shows the major physiographic features around the Tianwen-1 touch-down spot and the landing sites of previous missions, including the Viking Lander 2 (VL2), the InSight Lander, Mars Science Laboratory (MSL), the Mars Exploration Rover (MER-A) Spirit rover. The base map is a portion of the MOLA shaded-relief topographic map of Mars with elevations for the geoid. **b**, MOLA-derived elevation map of the Tianwen-1 surrounding region in a circular shape. The 20 km diameter circular map is centered at 109.925° E, 24.980° N, about 10 km south of the Tianwen-1 landing site. The average elevation is -4095 m in the region. **c**, The slope map of the Tianwen-1 surrounding region is based on the MOLA data (baseline 926 m). About 99% of the topography is flat (slopes $< 2.3^{\circ}$), and the area with more significant slopes ($> 2.3^{\circ}$) primarily distributes on the rim of the impact craters.

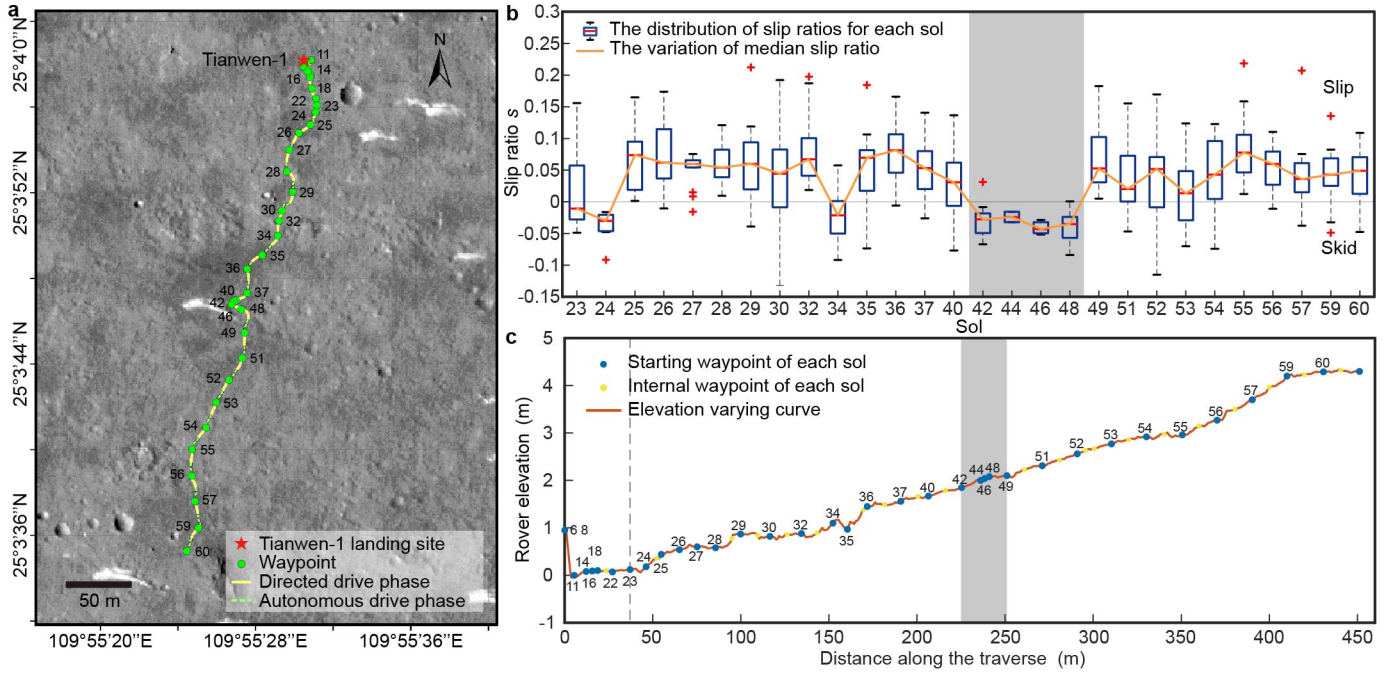


Fig. 2. The routing path of the Zhurong rover and the associated wheel slippage for the first 60 sols.

a, The routing path of the Zhurong rover. The green dots represent starting waypoint on each sol. The rover has passed through 55 waypoints during the first 60-sols operation. The base image is a high-resolution (~ 0.7 m/pixel) digital orthophoto map (DOM) generated from the High Resolution Imaging Camera (HiRIC) images taken by the Tianwen-1 orbiter. **b**, The box plot of wheel slip ratios of the Zhurong rover. Only the sols when Zhurong moves in high-efficiency mode (from sol 23 on) are plotted. Each box represents the distribution of wheel slip ratios over continuous traverses experienced in that sol. Traveling distances on sols 42-48 are short, causing relatively large locomotion measurement errors and resulting in the slip ratio in disagreement with the elevation trend. **c**, The elevation profile along the traversed path during the first 60 sols. The blue dots represent the rover elevation of starting waypoints on each sol, while the yellow dots represent the elevation within the waypoints. The rover elevation of waypoint X (the initial waypoint on the surface) is taken as the baseline (elevation of 0), and the elevation varies from 0 (on sol 10) to 4.34 (on sol 60) m.

5

10

15

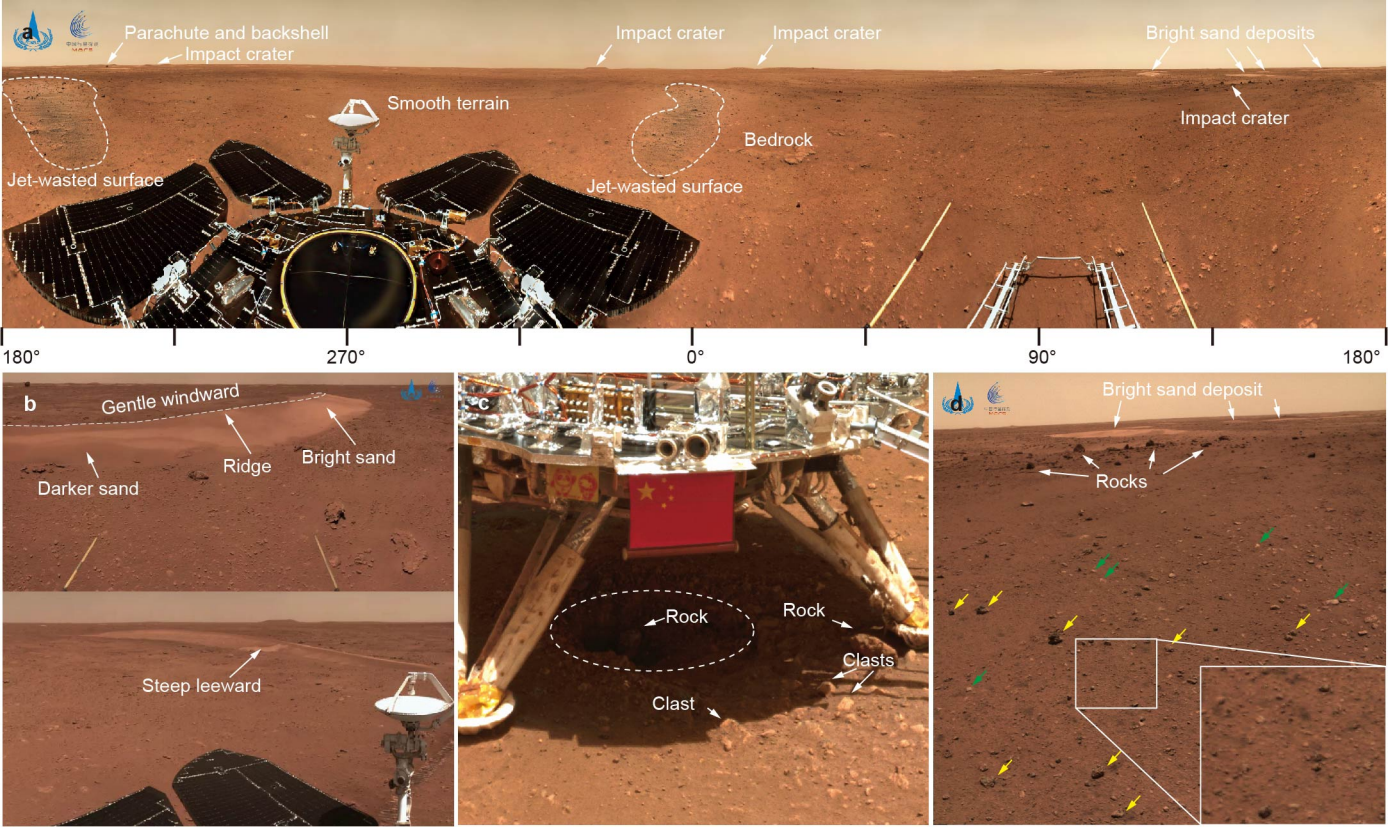


Fig. 3. The geological features at the landing site. **a**, The first 360° panorama of the Tianwen-1 landing site taken by the NaTeCam. The image is stitched by 12 images taken at 30° intervals by the NaTeCam on sol 6. The Zhurong rover is heading southwards, and the parachute and backshell are located a few hundred meters to the southwest of the lander. Two jet-wasted traces reveal darker materials below the topsoil. On the southeast of the lander, there are several bright sand dunes, a small crater surrounded by several dark-colored rocks, probably ejected from the crater. **b**, The first aeolian dune that Zhurong rover has encountered. The windward slope is relatively gentler than the leeward one. The image was taken on sol 50. **c**, A mini crater (~0.95 m in diameter) right underneath the lander formed by the thrust engine plume of the Tianwen-1 probe during landing. The crater reveals two distinct rock fragments. The one with a dark-brown tone contrasts sharply with the bright-tone clasts semi-buried in the soils and dust. **d**, Soil surface scattered with bright-toned clasts (green arrows) and small-sized dark-toned rocks (yellow arrows).

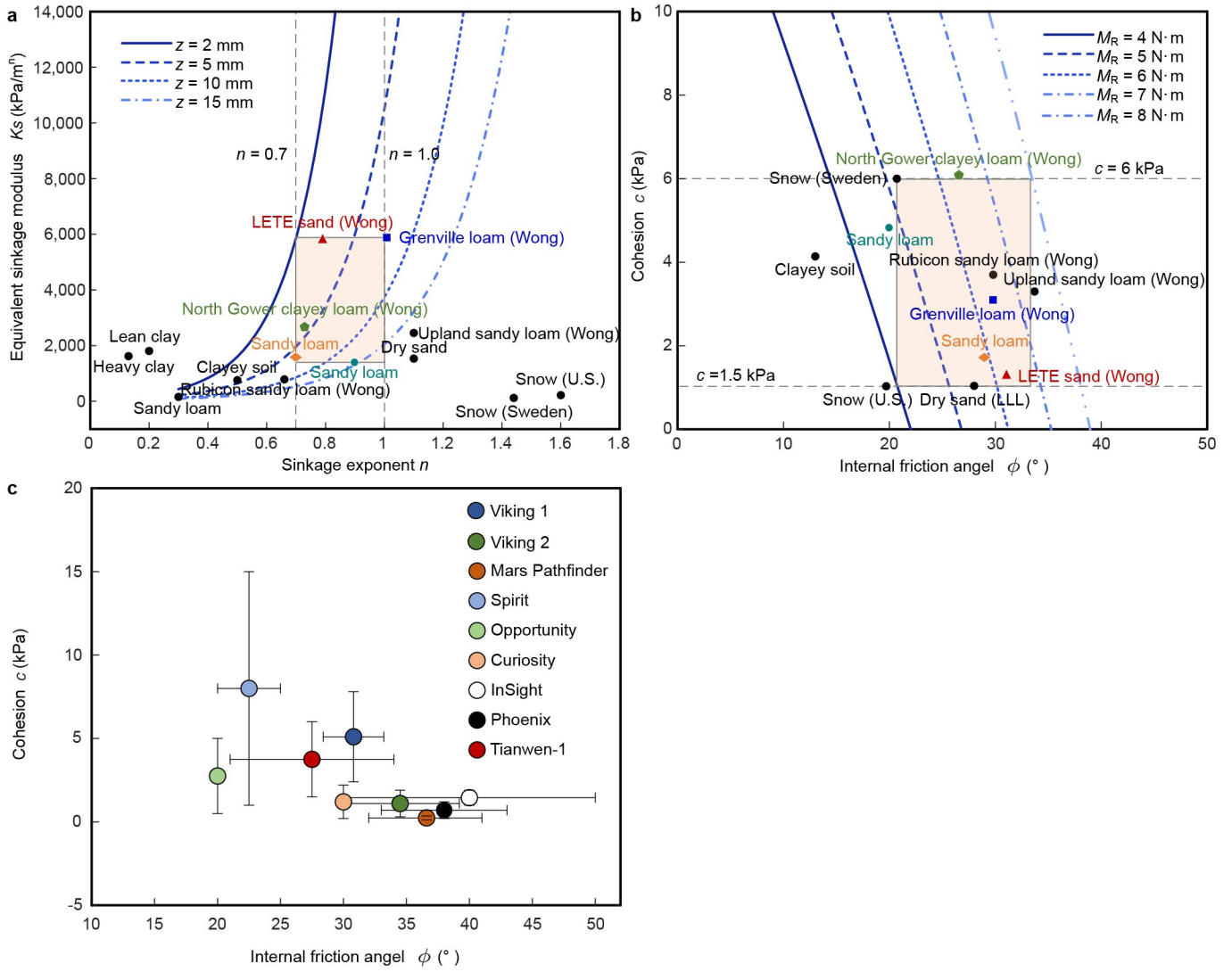


Fig. 4. Analysis of soil mechanical parameters at the Zhurong landing site. a, Soil bearing characteristic curves under different wheel沉降 for Zhurong's wheels and the bearing parameters of typical soil samples on Earth. The soil bearing properties at the Tianwen-1 landing site are close to representative soil samples on Earth, such as the LETE sand (Wong) (red triangle), Grenville loam (blue square), and North Gower clayey loam (Wong) (green pentagon). The bearing parameters of soil samples at the Tianwen-1 site are presumed to be within the area (in light orange) containing five soil samples it it. The bearing parameters of typical soil samples on Earth are listed in Supplementary Table 1. **b,** Soil shearing characteristic curves derived from rover driving torque for Zhurong's wheels and the shearing parameters of typical soil samples on Earth. The more significant driving torque used for traverse represents stronger shearing resistance of the soil. The shearing parameters of typical soil samples on Earth are listed in Supplementary Table 1. **c,** Soil shearing parameters of Tianwen-1 landing site compared with that of other Mars landing sites. The shearing parameters of soil samples on other Mars landing sites are listed in Supplementary Table 2.

Methods

Instruments and data description

The Zhurong rover is a six-wheeled solar-powered robot with active suspension. Benefited from its active suspension structure³², the rover is not only able to work in basic wheeled movement modes but also capable of novel gaits, such as a crab gait for cross-walking, a creeping gait for better slope climbing capability, a wheel uplift gait to escape from wheels being stuck³³, and a body uplift/settlement gait. The strong terrain adaptability and resilient fault recovery capability allow the rover to access dangerous but scientifically beneficial regions, such as sand dunes and crater rims, leading to significant scientific discoveries. The lugged wheels on the Zhurong rover are used as devices for soil mechanical parameter analysis based on terramechanics. Considering the gravity on Mars, the vertical load on each wheel is estimated to be 148.8 N under a quasi-static state, based on the rover's configuration and mass distribution. The parameters of the drum-shaped wheel are in the Extended Data Table 1.

The data used in this study includes images from a NaTeCam, two HazCams, and a wireless camera, alongside locomotion data from the onboard inertial measurement unit and wheel encoders.

The NaTeCam, one of the scientific payloads, is mounted on the mast of the Zhurong rover. It consists of two optical systems with identical functions, performances, and interfaces. The parameters of the NaTeCam are in the Supplementary Table 3. The NaTeCam is used for three-dimensional panoramic imaging of the Mars surface, and to study topography and geological structure of the roving area. It takes 12 pairs of images in sequence to compose a 360° global perception.

The HazCam and wireless camera are engineering payloads onboard the Zhurong rover. There are two pairs of separately installed HazCams at the front and back of the rover's carriage. The parameters of the HazCam are also in the Supplementary Table 3. The wireless camera is hidden at the bottom of the rover's carriage. It is equipped with WiFi components and has WiFi communication capabilities. The camera was

released at sol 17 to take a selfie of both the rover and the lander. There is also a WiFi receiving device on the lander responsible for receiving WiFi image data and transmitting it back to Earth.

The locomotion data used in this study included the rover's position (x , y and z) and posture (roll, pitch and yaw) at the landing site local (LSL) coordinate frame, the rover's velocities along three axes in its coordinate frame, and the angular velocities of each of the wheels. The rover's positions and postures are derived from the inertial measurement unit onboard, and the wheels' angular velocities are derived from the angle recorded by wheel encoders. The LSL coordinate frame is a north-east-down right-handed coordinate system with its origin at the first waypoint. Its z -axis points down in the local normal direction, the x -axis points to the north pole, and the y -axis is orthogonal to the x - and z -axes. The rover coordinate frame is an east-north-up right-handed local system, whose origin is at the rover's centre, its x -axis points to the forward direction of the rover, its z -axis points in the local normal direction, and its y -axis is orthogonal to the x - and z -axes. These data were recorded onboard at a higher frequency, but the data transmitted to Earth are only at a frequency of 1/15 Hz due to the communication channel restriction, with both recorded and received timestamps.

15 **Wheel slip ratio estimation based on telemetry data**

The slip ratio s of a lugged wheel at each moment t is defined as follows:

$$s(t) = \begin{cases} 1 - v(t)/(r_s \omega(t)) & (r_s \omega(t) \geq v(t), 0 \leq s(t) \leq 1) \\ r_s \omega(t)/v(t) - 1 & (r_s \omega(t) < v(t), -1 \leq s(t) < 0) \end{cases}, \quad (1)$$

where $\omega(t)$ is the angular velocity function, r_s is the shearing radius function, and $v(t)$ is the linear velocity function. The wheel angular velocity is recorded by wheel encoders, and its linear velocity is derived based on the rover's linear velocity (recorded by the onboard inertia measurement unit) and the curvature of the trajectory. The shearing radius r_s can be computed as³⁴:

$$r_s = r + \lambda_s h, \quad (2)$$

where r is wheel radius, h is the lug height and λ_s ($1 \leq \lambda_s \leq 0$) is the lug coefficient determined by the number of lugs and the internal friction angle of the soil. As Zhurong's wheels are drum-shaped, its radius r in equation (2) is set as a value between the largest radius and the smallest radius. Here, it is set as the mean of wheel's largest radius and its smallest radius. Besides, Zhurong's wheels are with evenly arranged 5mm-high lugs, thus the value of λ_s is approximately 0.5 according to the experiment results in 34.

A slip ratio s value larger than zero indicates that the wheel has slipped; an s equal to 0 indicates that the wheel has rolled without slipping or skidding; and an s less than 0 indicates that the wheel has skidded, with $|s|$ being the values of the skid ratio. Generally, a driving wheel slips when moving on flat terrain or climbing up a slope, and may skid when moving down a slope³³.

10 Slip ratio estimation based on wheel imprint

The slip ratio of a Zhurong rover wheel can be estimated from the imprint of the wheel. A clear and intact wheel imprint with a longitudinal slip, as shown in Extended Data Fig. 4a, consists of a series of trace units, whose width is denoted by Δx_p , and each trace unit can be divided into two areas: the lug-sheared area dug out by the lug itself and the hub-pressed area compressed by the wheel hub. Through analysis of the formation mechanism of wheel track imprints with longitudinal slip, the relationship of the average wheel slip ratio \bar{s} and the width of the trace unit Δx_p can be deduced as³⁵:

$$\bar{s} = 1 - \Delta x_p n / (2\pi r_s) \quad (0 \leq \bar{s} \leq 1), \quad (3)$$

where n is the number of lugs on the wheel. Therefore, \bar{s} can be estimated by measuring Δx_p .

The width of the trace unit Δx_p is estimated using NaTeCam or rear HazCam images (Extended Data Fig. 4b, c). An image processing method was introduced to extract Δx_p with two key steps: view correction and trace feature extraction. The original image is first corrected with the camera extrinsic matrix to a top-view image. Then, each trace imprint unit is manually divided into independent areas, and trace imprint

information, such as the trace unit width, is acquired. The wheel slip ratio is then estimated from the trace imprint using equation (3). When a series of continuous trace units has almost the same width, the average trace unit widths are calculated to reduce the measurement error, and the average wheel slip ratio is deduced to represent the wheel slippage experienced by Zhurong. Since only whole imprints of the rear wheels are left behind the rover while the front and the middle wheel imprints are typically overlapped, the slip ratio of the rear wheels was estimated to represent the rear wheel slippage at the respective moment.

Soil parameter analysis

Zhurong's wheels were used as devices to analyze soil parameters based on wheel-soil interaction. For a lugged rover wheel moving on the soil with an angular velocity ω , the wheel is applied with a vertical load W and a resistance force f_{DP} from the vehicle suspension, as well as a driving torque T at the wheel rotational axis by an actuator. The terrain interacts with the wheel circumference in the contact region, which corresponds to the angle divided into two parts: the entrance angle θ_1 from the vertical at which the wheel first makes contact with the soil, and the exit angle θ_2 from the vertical, at which the wheel loses contact with the soil. In the wheel-terrain interaction region ($\theta_1+\theta_2$), the continuous normal stress σ to support the wheel, and the shearing stress τ due to the relative movement are exerted on the wheel surface, as shown in Extended Data Fig. 7a. The point of maximum stress is denoted as θ_m , according to which the stress region is divided into a forward part (σ_1, τ_1) , corresponding to the angle from θ_1 to θ_m , and a rear part (σ_2, τ_2) , corresponding to the angle from θ_m to θ_2 .

The soil bearing parameters are closely related to the wheel-soil interaction in the normal direction. Considering the shape of the wheel surface, the distributed normal stress³⁶ along the wheel circumference deduced from the Reece-Wong model³⁷ is

$$\begin{cases} \sigma_1(\theta) = \left(\frac{k_c}{b} + k_\phi\right) r_s^n (\cos \theta - \cos \theta_1)^n & (\theta_m \leq \theta < \theta_1) \\ \sigma_2(\theta) = \left(\frac{k_c}{b} + k_\phi\right) r_s^n \left\{ \cos \left[\theta_1 - \frac{\theta - \theta_2}{\theta_m - \theta_2} (\theta_1 - \theta_m) \right] - \cos \theta_1 \right\}^n & (\theta_2 \leq \theta < \theta_m) \end{cases}, \quad (4)$$

where b is the width of the wheel, r_s is the equivalent wheel radius calculated on equation (2), k_c is the cohesive modulus of the soil, k_ϕ is the frictional modulus of the soil, and n is a soil sinkage exponent that can be represented by a linear function of slip ratio s as follows:

$$5 \quad n = n_0 + n_1 s, \quad (5)$$

where n_0 represents the static sinkage exponent and n_1 represents the dynamic sinkage resulting from wheel slippage. The values of n_0 and n_1 are determined based on experiments, and the introduction of the linear soil sinkage exponent leads to a high affinity for fitting the slip-sinkage phenomenon of lugged wheels¹⁴.

The entrance angle θ_1 is a function of wheel sinkage z as:

$$10 \quad \theta_1 = \arccos[(r - z) / r], \quad (6)$$

and the exit angle θ_2 is computed as:

$$\theta_2 = c_3 \theta_1, \quad (7)$$

where c_3 is a coefficient of the wheel-terrain interaction angle, generally assumed to be 0^{38} . The exit angle θ_2 is used to compute the stress caused by the rebound of the soil (stress integration from θ_m to θ_2), which is 15 usually negligibly small and is taken as zero in the calculation.

The maximum stress angle θ_m is computed as:

$$\theta_m = (c_1 + c_2 s) \theta_1, \quad (8)$$

where c_1 and c_2 are coefficients of the wheel-terrain interaction angle. In the calculation, c_1 and c_2 are set to 0.5 and 0, respectively, because it is reasonable to assume that the angular location of maximum stress θ_m occurs midway between θ_1 and θ_2 ³⁹.

The tangential stress $\tau(\theta)$ is computed as

$$\tau(\theta) = (c + \sigma(\theta) \tan \phi) \times \left\{ 1 - \exp(-r_s [(\theta'_l - \theta) - (1-s)(\sin \theta'_l - \sin \theta)] / k) \right\}, \quad (9)$$

where c is the cohesion of the soil, ϕ is the internal friction angle, k is the shearing deformation modulus, r_s is the equivalent shearing radius calculated on equation (2), and θ'_l is the equivalent entrance angle. With
5 the lug effect, the shearing stress occurs on the surface of the soil sticking to the wheel circumference due to the wheel lugs instead of the wheel outer cylinder surface. The equivalent entrance angle θ'_l of a lugged wheel¹⁴ is computed as

$$\theta'_l = \arccos[(r - z) / (r + h)]. \quad (10)$$

When θ approaches θ_m , the corresponding normal stress and tangential stress approach their maximum as
10

$$\sigma_m = \left(\frac{k_c}{b} + k_\phi \right) r^n (\cos \theta_m - \cos \theta_l)^n, \quad (11)$$

$$\tau_m = (c + \sigma_m \tan \phi) \times \left\{ 1 - \exp(-r_s [(\theta'_l - \theta_m) - (1-s)(\sin \theta'_l - \sin \theta_m)] / k) \right\}. \quad (12)$$

When the wheel is in a quasi-static state, the effect of the distributed stress (normal stress σ and tangential stress τ) can be simplified to the normal force F_N , drawbar pull F_{DP} , and driving resistance torque M_R by integrating along with the wheel–terrain interaction area, which are balanced with the wheel load W ,
15 resistance force f_{DP} , and driving torque T , respectively. For the wheels of Zhurong moving almost on flat terrain with a maximum speed of 200 m/h, the quasi-static condition is valid because the dynamic effects are negligible at low speeds. Therefore, the force/torque balance equations for Zhurong's lugged wheels can be expressed as follows:

$$F_N = b \left\{ \int_{\theta_2}^{\theta_m} [r\sigma_2(\theta) \cos \theta + r_s \tau_2(\theta) \sin \theta] d\theta + \int_{\theta_m}^{\theta_l} [r\sigma_1(\theta) \cos \theta + r_s \tau_1(\theta) \sin \theta] d\theta \right\} = W, \quad (13a)$$

$$F_{DP} = b \left\{ \int_{\theta_2}^{\theta_m} [r_s \tau_2(\theta) \cos \theta - r\sigma_2(\theta) \sin \theta] d\theta + \int_{\theta_m}^{\theta_l} [r_s \tau_1(\theta) \cos \theta - r\sigma_1(\theta) \sin \theta] d\theta \right\} = f_{DP}, \quad (13b)$$

$$M_R = r_s^2 b \left[\int_{\theta_2}^{\theta_m} \tau_2(\theta) d\theta + \int_{\theta_m}^{\theta_1} \tau_1(\theta) d\theta \right] = T \quad (13c)$$

According to Shibly et al.³⁹, the wheel-terrain interaction stress can be linearized as follows:

$$\begin{cases} \sigma_1(\theta) = \sigma_m (\theta_1 - \theta) / (\theta_1 - \theta_m) & (\theta_m \leq \theta \leq \theta_1) \\ \sigma_2(\theta) = \sigma_m (\theta - \theta_2) / (\theta_m - \theta_2) & (\theta_2 \leq \theta \leq \theta_m) \end{cases}, \quad (14)$$

$$\begin{cases} \tau_1(\theta) = \tau_m (\theta_1 - \theta) / (\theta_1 - \theta_m) & (\theta_m \leq \theta \leq \theta_1) \\ \tau_2(\theta) = \tau_m (\theta - \theta_2) / (\theta_m - \theta_2) & (\theta_2 \leq \theta \leq \theta_m) \end{cases}. \quad (15)$$

Because the entrance angle is usually not large, and when θ approaches θ_1 , the corresponding normal stress and tangential stress all approach zero, Ding⁴⁰ proposed that the product of $\cos\theta$ and stress can also be linearized. Let $\sigma'_m = \sigma_m \cos\theta_m$ and $\tau'_m = \tau_m \cos\theta_m$. Then, it can be deduced that

$$\begin{cases} \sigma_1(\theta) \cos\theta = \sigma'_m (\theta_1 - \theta) / (\theta_1 - \theta_m) \\ \sigma_2(\theta) \cos\theta = \sigma'_m (\theta - \theta_2) / (\theta_m - \theta_2) \end{cases}, \quad (16)$$

$$\begin{cases} \tau_1(\theta) \cos\theta = \tau'_m (\theta_1 - \theta) / (\theta_1 - \theta_m) \\ \tau_2(\theta) \cos\theta = \tau'_m (\theta - \theta_2) / (\theta_m - \theta_2) \end{cases}. \quad (17)$$

Bringing equations (16)~(17) into the wheel-terrain interaction model of equation (13a), and ignoring the vertical component of the shearing stress, we can obtain simplified expressions⁴⁰ of the normal force F_N and the driving torque M_R as

$$F_N \approx rb(\theta_1 - \theta_2) \sigma_m \cos\theta_m / 2, \quad (18)$$

$$M_R = r_s^2 b(\theta_1 - \theta_2) \tau_m / 2, \quad (19)$$

while equation (18) and equation (19) can be rearranged as

$$\sigma_m = \frac{2F_N}{rb(\theta_1 - \theta_2) \cos\theta_m}, \quad (20)$$

$$\tau_m = \frac{2M_R}{r_s^2 b(\theta_1 - \theta_2)}. \quad (21)$$

Equation (20) is combined with equation (11) to obtain the relationship of bearing characteristic parameters (cohesive modulus k_c , frictional modulus k_ϕ , and sinkage exponent n of the soil). When the normal force F_N and the wheel沉降 z are estimated while the wheel parameters are known, let
5 $K_s = k_c/b + k_\phi$, then the bearing characteristics curves of the soil for the sinkage exponent n and the equivalent stiffness modulus K_s under different wheel sinkages can be plotted as in Fig. 4a.

Regarding the analysis of the soil shearing parameters, we find equations (12) and (21) are two expressions of the maximum tangential stress τ_m , and the maximum shearing stress τ_m can be directly calculated according to equation (21), with the measured driving resistance torque M_R . Then, all quantities
10 in equation (12) can be measured except for the three unknown shearing parameters (the cohesion c , the internal friction angle φ , and shearing deformable modulus k). The shearing deformable modulus k is determined by the slope of the shearing curve at the origin point and the maximum tangential stress τ_m . Its value is 1/3 of the corresponding shearing deformation when the shearing stress τ is equal to 95% of the maximum shearing stress τ_m . The denser the soil, the smaller the value of k . We concluded in the main text
15 that Martian soil at the Tianwen-1 landing site has a larger bearing strength than the lunar regolith. The typical value of the shearing deformable modulus k of the lunar regolith is 17.8 mm, therefore it is assumed here that the soil shearing deformable modulus k at the Zhurong landing site is 5 mm. Since the soil parameters at the Zhurong landing site have not been rigorously identified, a value of k of 5 mm is not accurate, but it can be used for inference. Therefore, the shearing characteristics curves of the soil for the
20 cohesion c and the internal friction angle φ under different driving torques can be plotted.

In practice, the values of the wheel radius r , wheel width b , wheel lug height h , and equivalent radius r_s are constant and determined by Zhurong's wheel configuration, as shown in Extended Data Table 1. The normal force F_N is estimated from the vertical load W , which can be computed from a quasi-static force

analysis of the rover with knowledge of the rover configuration and mass distribution. The two key wheel motion state indicators, the slip ratio s and sinkage z , can be computed using vision-based techniques or kinematic analysis of the rover suspension. Based on the given parameters, for wheel sinkages of 2, 5, 10, and 15 mm, the curves of the equivalent stiffness modulus (denoted by K_s) and the sinkage exponent n were plotted (Fig. 4a). The motor current of the driving wheel varied from 0.17 A to 0.28 A with an average of 0.23 A when the wheel was rotating. Using the relationship between the motor current and the driving torque for the driving wheel, as shown in Extended Data Fig. 7b and the reduction ratio of the reduction drive between the wheel driving motor and the driving wheel (3.92×160 with an efficiency of 60%), the driving torque was calculated to be $3.7\sim7.0$ N·m, and the average driving torque for each continuous steady traverse could be calculated for analysis. The maximum and minimum average driving torques are 3.7 N·m and 7.0 N·m, respectively. The average driving torque is mostly around 5.5 N·m. Therefore, for driving torques of 4, 5, 6, 7, and 8 N·m, the curves of the cohesion c and the internal friction angle φ were plotted (Fig. 4b).

References

- 15 32. Zheng, J. *et al.* Design and terramechanics analysis of a Mars rover utilizing active suspension. *Mech. Mach. Theory* **128**, 125–149 (2018).
33. Gao, H., Zheng, J., Liu, Z., Yu, H., Ding, L., Li, N., Deng, Z. Performance analysis on wheels lifting-off-ground for Mars rover with active suspension, *Robot* **39**, 139–150 (2017).
34. Ding, L., Gao, H., Deng, Z., Yoshida, K., Nagatani, K. paper presented in the 2009 IEEE/RSJ
20 International Conference on Intelligent Robots and Systems, St. Louis, MO, USA, 10 to 15 October
2009.
35. Li, N. thesis, Harbin Institute of Technology (2019).

36. Ding, L., Gao, H., Liu, Z., Deng, Z. & Liu, G. Identifying mechanical property parameters of planetary soil using in-situ data obtained from exploration rovers. *Planet Space Sci.* **119**, 121–136 (2015).
37. Bekker, M. G. *Introduction to Terrain-Vehicle Systems, Part I: The Terrain. Part II: The Vehicle* (Michigan Univ Ann Arbor, Ann Arbor, MI, 1969).
- 5 38. Terzaghi, K., Peck, R. B., Mesri, G. *Soil Mechanics in Engineering Practice* (John Wiley & Sons, New Jersey, 1996).
39. Shibly, H., Iagnemma, K., Dubowsky, S. An equivalent soil mechanics formulation for rigid 25 wheels in deformable terrain, with application to planetary exploration rovers, *J. Terramech.* **42**, 1–13 (2005).
40. Ding, L. thesis, Harbin Institute of Technology (2009).

10 **Data availability:** Datasets generated or analysed during this study are available from the corresponding authors upon reasonable request.

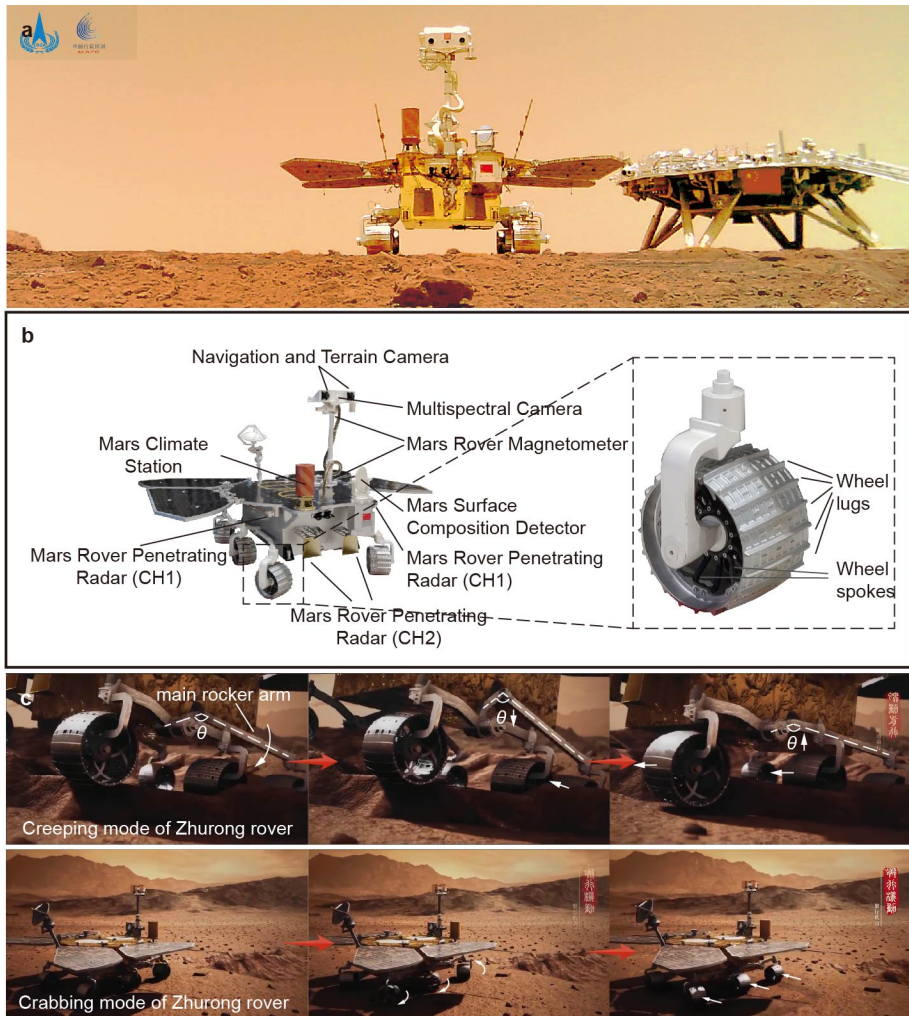
Acknowledgments: This work was supported in part by the Development Program of China under Grant 2019YFB1309500, in part by the National Natural Science Foundation of China under Grant 51822502 and Grant 91948202, in part by the ‘111 Project’ under Grant B07018, in part by the Heilongjiang Postdoctoral Fund under Grant LBH-Z20136, in part by the Self-Planned Task of State Key Laboratory of Robotics and System (HIT) under Grant SKLRS 202101A03, and in part by the Pre-research project on Civil Aerospace Technologies by CNSA under Grant D020102.

Author contributions: L. Ding coordinated; and wrote the manuscript with R. Zhou. T. Yu led the Zhurong rover operation and data acquisition. H. Gao and H. Yang coordinated coauthor contributions.
20 Data and image analysis: L. Ding, R. Zhou, H. Gao, H. Yang, Y. Yuan, Z. Wang, Z. Deng, L. Huang, N. Li, Z. Li, F. Niu, H. Qi, S. Li, W. Feng, C. Yang, H. Xing, G. Wang, L. Niu, P. Xu. Rover operations and data acquisitions: T. Yu, J. Li, C. Liu, J. Wang, X. Cui, X. He, H. Zhang, R. Zhao, Z. Zhang, Z. Cheng, F. Wu, Q. Xu, H. Lu, L. Li, X. Wang, Z. Huang, J. Zhang. Rover parameters provision and analysis: Y. Jia, B.

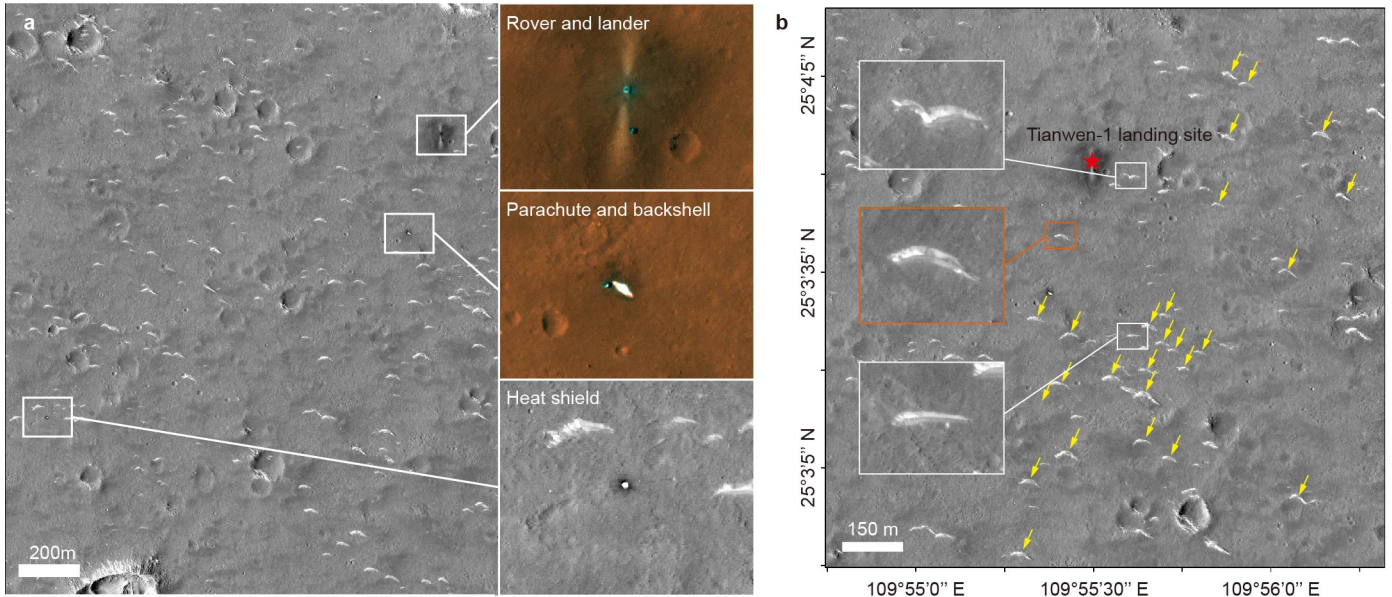
Yuan, B. Chen, Z. Dang. Geological analysis and interpretation: Y. Zhao, X. Wang, G. Bao, W. Wan, M. Zhang, K. Di. Results and writing refinement: G. Liu and L. Richter. All authors reviewed and revised the manuscript.

Competing interests: The authors declare that they have no competing interests.

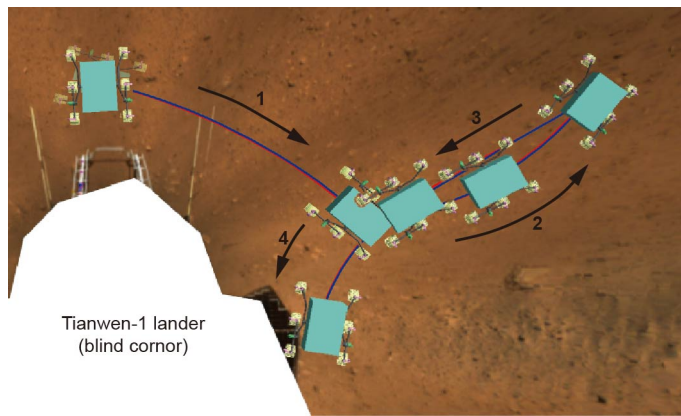
5 **Additional Information: Supplementary Information** is available for this paper. Correspondence and requests for materials should be addressed to L. Ding (email: liangding@hit.edu.cn), or H. Gao (email: gaohaibo@hit.edu.cn) or H. Yang (email: yanghuaiguang@hit.edu.cn).



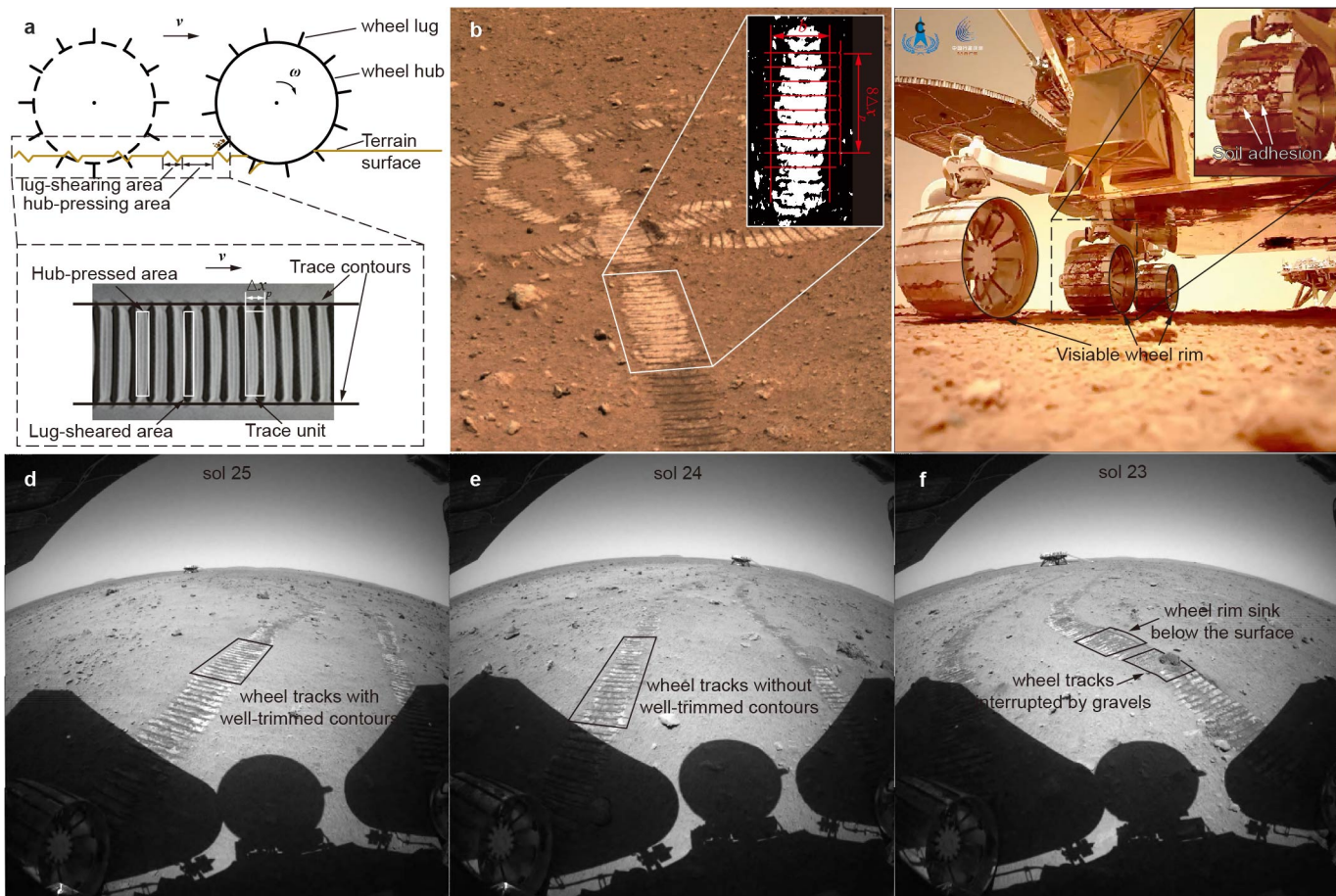
Extended Data Fig. 1. Zhurong rover on Tianwen-1 mission. **a**, The first group photo of Zhurong rover and Tianwen-1 lander on the Martian surface. The image was taken by a wireless camera deployed by Zhurong on sol 18 (June 1, 2021). **b**, Six scientific payloads and the lugged wheel on the Zhurong rover. The six scientific payloads² include NaTeCam, Multispectral Camera (MSCam)³, Mars Rover Penetrating Radar (RoPeR)⁴, Mars surface Composition Detector (MarSCoDe)⁷, Mars Rover Magnetometer (RoMAG)⁶, and Mars Climate Station (MCS)⁵. The lugged wheel is evenly arranged with 20 lugs on its outer surface and spokes inside. **c**, Creeping and crabbing mode of Zhurong rover relied on active suspension joints. The creeping mode of Zhurong to get out of sunk and climb steep slopes is realized by decreasing or increasing the angle of the main rocker arm, coordinated with the movement of other wheels. The crabbing mode of Zhurong for lateral movement is achieved by turning the steering wheels at 90° and driving laterally.



Extended Data Fig. 2. HiRISE image of Tianwen-1 probe. The HiRISE image is ESP_06937_2055 at 29.2 cm/pixel (with 1×1 binning) acquired by NASA's Mars Reconnaissance Orbiter on June 2, 2021. **a**, A regional view of the location of the Tianwen-1 lander, Zhurong rover, parachute and backshell, and heatshield. The backshell and parachute are located at 109.923° N, 25.059° E, ~350 m (Northing = 330.6 m, Easting = 114.7 m) in the southwest of the lander. The heatshield is located at 109.901°N, 25.048°E, ~1617 m (Northing=1307.4 m, Easting=944.5 m) southwest from the lander. In the close up color image, the large bright spot is the lander of Tianwen-1, while the small bright spot is the Zhurong rover. There are symmetrical bright radial streaks of jets in the north-south direction centered on the lander, which might be due to the engine plume during landing blowing away the original surface materials. The backshell is of the round bright spot and the parachute is of the long bright spot. The close up of the heatshield is shown in the panchromatic image. **b**, Distribution and characteristics of dunes around the Tianwen-1 landing site on Mars. The three enlarged views show three types of sand dunes in shapes: the seagull shape, the crescent shape and the line shape. Most dunes in this area are in a crescent shape and their windward slopes are (yellow arrows) oriented to the NE-SW direction.



Extended Data Fig. 3. Rover locomotion simulation. Simulation of four traverses after the rover driving off the ramp is visualized. The red line represents the planned path and the blue line represents the path obtained in simulation. The movement sequence of the rover is carried out in the order of the number marked. The terrain map is built from NaTeCam images.

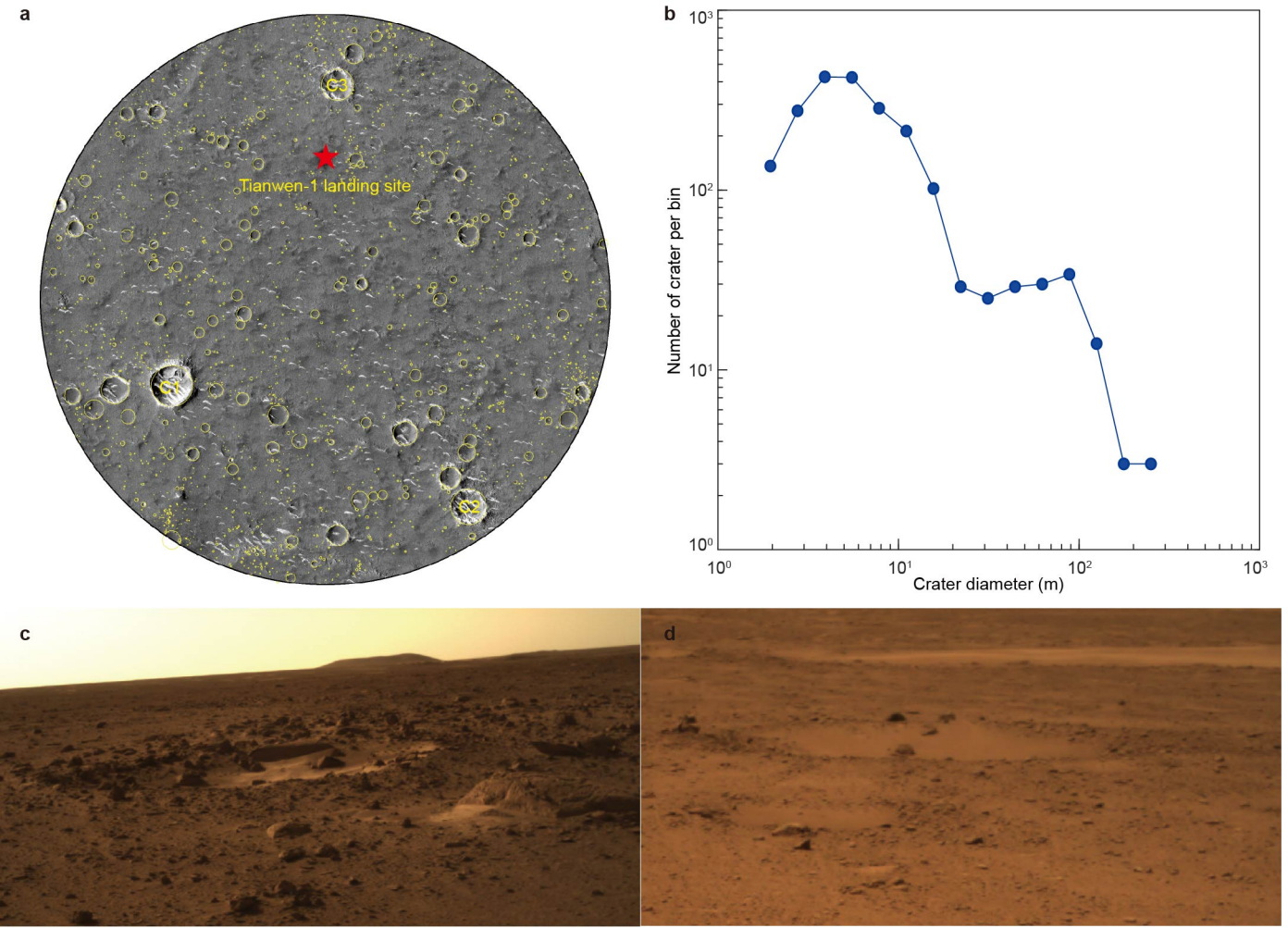


Extended Data Fig. 4. Wheel track analysis. **a**, Staggered pattern of the wheel track left by a wheel moving with longitudinal slip. **b**, Wheel track extraction and wheel slip ratio analysis over a traverse to waypoint A. Eight continuous track units are extracted on the orthograph for local wheel slip ratio calculation. The image was taken by the NaTeCam on sol 11. **c**, Near-Side view of the wheel-terrain interaction. Only wheel lugs are submerged into the soil and the wheel rims of these three right wheels are millimetres above the surface. Some soil adhered to the wheel surface or on the groove bordering the lugs. This image was taken by the wireless camera on sol 12 when the rover was retreating. **d**, **e**, **f**, show wheel tracks and the associated wheel sinkage. Images were taken by the rear HazCam. **d**, A part of legible wheel track with well-trimmed contours. The wheel沉降 is estimated to be about 10 mm. **e**, Most common form of wheel tracks without well-trimmed contours. Its wheel沉降 is estimated to be ~5 mm. **f**, shows both wheel tracks interrupted by gravels and wheel tracks with rim sinking below the surface. The wheel沉降 of the wheel tracks interrupted by gravels is estimated to be ~2 mm. The wheel沉降 of wheel tracks formed by the wheel rim sinking below the surface is estimated to be ~15 mm.

5

10

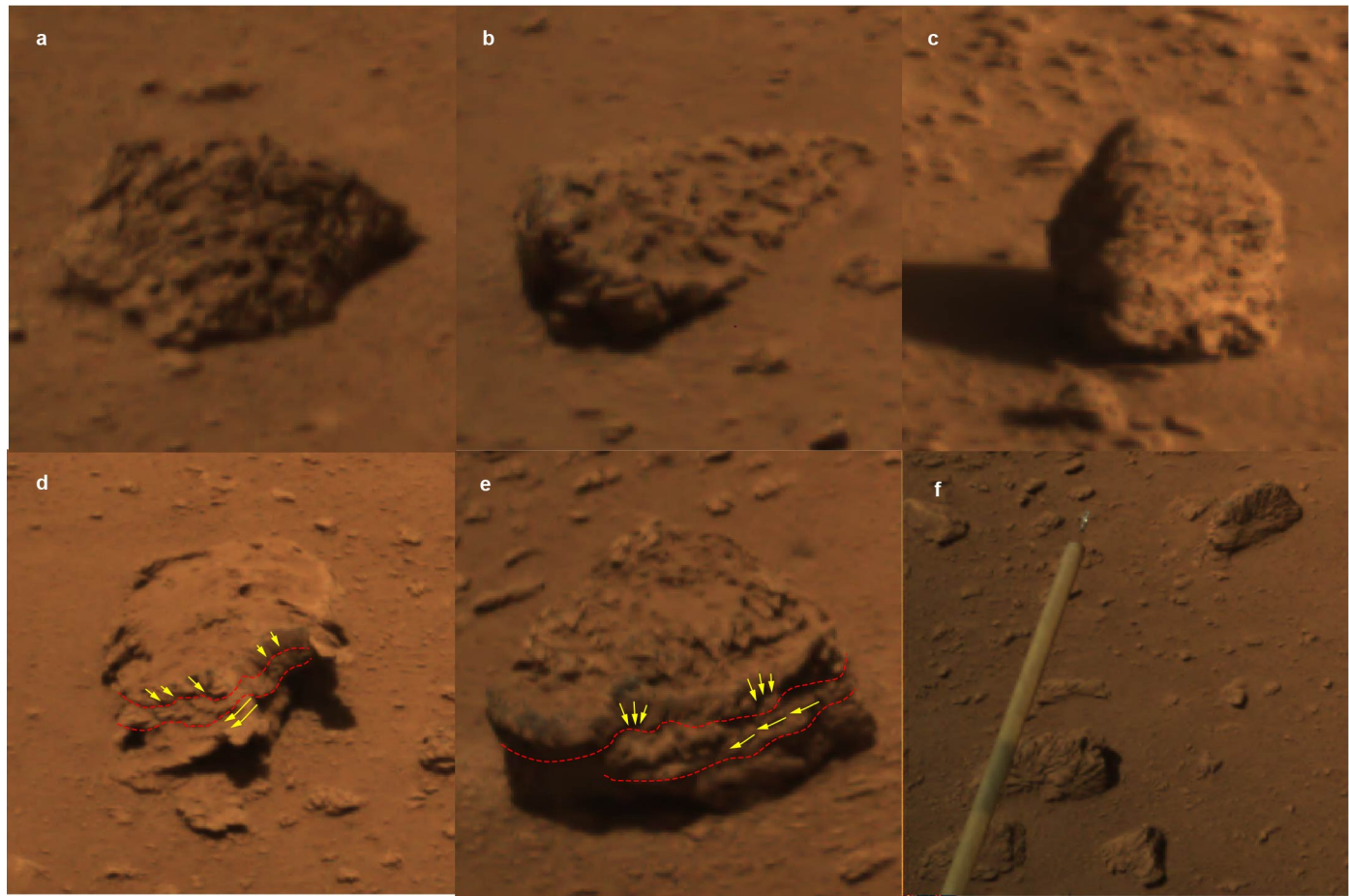
15



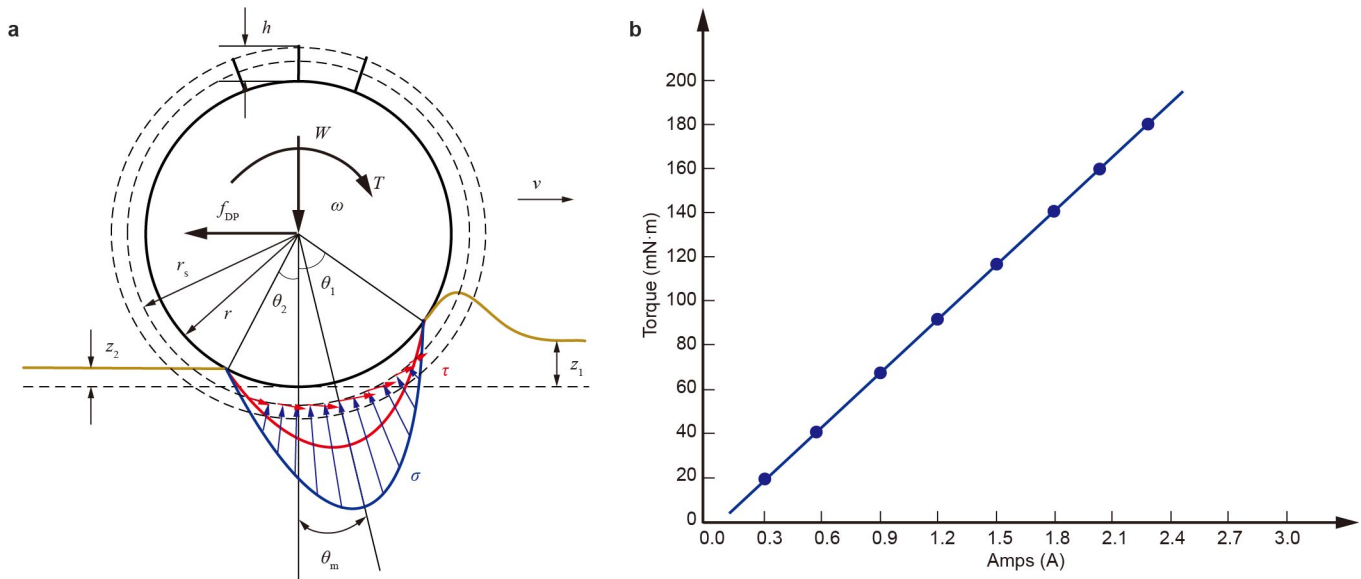
Extended Data Fig. 5. Craters around the Tianwen-1 landing site. **a**, The distribution of the mapped craters (diameters > 1 m) in the circular region surrounding the Tianwen-1 landing site, overlaid on the HiRISE image (ESP_06937_2055). C1, C2, C3 are three large craters (diameter > 200 m) in this area. The circular region is centred on 109.925° E, 25.048° N with a diameter of 3 km, and its centre is 1 km south away from Tianwen-1 landing site. **b**, A log-log plot of the incremental size-frequency distribution of craters. The diameter interval is $\sqrt{2} D$ m and the crater diameter refers to the middle value of each bin. **c**, A small crater surrounded by rocks in dark color with sand deposited at its bottom. The image was taken by NaTeCam on sol 34 (June 17, 2021). **d**, A crater suffered severe erosion, showing severely damaged rims and lose clear impact structure but present as the depression. The image was taken by NaTeCam on sol 57 (July 11, 2021).

5

10



Extended Data Fig. 6. Rocks around the Tianwen-1 landing site. a,b,c, are rocks riddled with small dense pits on the surface. The rocks appear relatively light in tone through the exposed surface with less dust and soil covering. d,e, are rocks showing layered structures, and about three layers (divided by red dash lines) can be seen on the sides. The rock flakes of the top layer and the middle layer seem different in direction. f, shows rocks with one windward face full of grooves, likely worn and shaped by wind-blown particles.



Extended Data Fig. 7. Wheel-soil interaction model and the driving motor characteristics curve. a, Force diagram for the wheel-soil interaction of a lugged wheel. **b,** Characteristics curve of the driving torque and the motor current for the driving motor on the Zhurong rover.

Extended Data Table 1. The parameters of the Zhurong rover.

Group	Parameter name	Value
Rover	Mass m (kg)	240
	Size $l \times w \times h$ (m)	1230×830×540
	Number of wheel	6
	Maximum driving speed v_{\max} (m/h)	200
	Maximum climbable slope on rigid ground ($^{\circ}$)	≥ 30
	Maximum climbable slope on soft ground ($^{\circ}$)	≥ 20
	Climbable obstacle (mm)	≥ 300
Lifting range of the rover body (mm)		0~500
Wheel	Maximum wheel radius r_{\max} (m)	0.145
	Minimum wheel radius r_{\min} (m)	0.135
	Wheel width b (m)	0.20
	Height of the wheel lug h (m)	0.005
	Number of wheel lugs	20
	Shearing radius of a wheel r_s (m)	0.146
	Normal force on each wheel F_N (N) (under quasi-static state)	148.8
	Wheel slip ratio s	-0.1~0.2
Wheel sinkage z (m)		0.005~0.01

Six wheels on the Zhurong rover can both driving and steering. The wheel's largest radius (145 mm) is in the middle cross-section and the smallest radius (135 mm) is on the two end faces at both sides. The 20 wheel lugs are evenly attach to the outer edge of the wheel.

Extended Data Table 2. Daily scientific exploration events. Zhurong carried out routine navigation and detection using NaTeCam, Mars rover penetrating radar (RoPeR), and Mars climate station (MCS) on most sols. Scientific payloads² like multispectral camera (MSCam), Mars surface composition detector (MarsSCoDe), and Mars rover magnetometer (RoMAG) are used for a specific target detection, like rocks and sand dunes. The *sol* represents a Martian day, corresponding to 24.65 hours at the early stage of the mission after landing.

Sol	Date	Accumulated mileage (m)	Key events
1 5-8	May 15 May 19-22	0 5.48	<ul style="list-style-type: none"> Landing successfully at Utopia Planitia Panoramic imaging and drive off the ramp
9-11	May 23-25	12.24	<ul style="list-style-type: none"> Panoramic imaging and discovery of parachute and backshell Wheel track imaging by the rear hazard avoidance camera Coarse landing site localization based on vision Wind measurements Moving to waypoint A with routine navigation and detection
12-16	May 26-30	18.73	<ul style="list-style-type: none"> Moving to waypoint B with routine navigation and detection Imaging the Chinese flag on the lander by Zhurong's TeNaCam Two descent images are transmitted back to Earth Dropping the wireless camera and take test shots
18	June 1	27.16	<ul style="list-style-type: none"> Group imaging of the lander and the rover Fine landing site localization based on descent images High resolution imaging of the orbiter observed the lander, rover, parachute, backshell and heatshield Routine navigation and detection
22	June 5	37.19	<ul style="list-style-type: none"> Multi-spectral imaging on a rock full of holes Surface composition detection on a rock and the soil Routine navigation and detection
23-44	June 6-28	238.42	<ul style="list-style-type: none"> Switching the rover locomotion mode to high efficiency mode Moving toward north to find the parachute and backshell with routine navigation and detection
45-46	June 29-30	241.02	<ul style="list-style-type: none"> Moving approach to a sand dune and taking near-field images with routine navigation and detection Sand dune in-situ detection using the multi-spectral camera and the surface composition detector
48 49 51-57	July 2 July 3 July 5-11	251.07 271.09 410.02	<ul style="list-style-type: none"> Moving toward north to find the parachute and backshell with routine navigation and detection Observation of a special rock Moving toward north to find the parachute and backshell with routine navigation and detection
59 60	July 13 July 14	430.72 450.86	<ul style="list-style-type: none"> Group imaging the parachute and backshell Moving to a nearby sand dune with routine navigation and detection

Extended Data Table 3. Driving motor current and wheel driving torque of traverses on sol 23-34.

Earth Data	Sol	Drive Distance (m)	Driving Motor Current (A)		Wheel Driving Torque (N·m)		Average Wheel Slip Ratio
			Average	Maximum	Average	Maximum	
June 6, 2021	23	5.03	0.28	0.35	7.0	9.1	0.02
June 8, 2021	25	5.30	0.17	0.22	3.7	5.0	0.07
June 10, 2021	27	8.12	0.25	0.33	5.9	8.5	0.06
June 11, 2021	28	9.13	0.24	0.39	6.0	10.3	0.07
June 12, 2021	29	9.64	0.25	0.41	6.1	10.9	0.06
June 13, 2021	30	9.82	0.20	0.28	4.6	6.8	0.05
June 15, 2021	32	8.83	0.22	0.33	5.0	8.5	0.09

The wheel driving torque is transformed from the driving motor current, considering the reduction rate and efficiency.

Supplementary Files

This is a list of supplementary files associated with this preprint. Click to download.

- [SupplementaryInformation.docx](#)